energies

MDPI

Article

Switching Sequence Model Predictive Direct Torque Control of IPMSMs for EVs in Switch Open-Circuit Fault-Tolerant Mode

Ting Yang [1,2], Takahiro Kawaguchi [1], Seiji Hashimoto [1,*] and Wei Jiang [3]

[1] School of Science and Technology, Gunma University, Kiryu, Gunma 376-8515, Japan; yt871028@163.com (T.Y.); kawaguchi@gunma-u.ac.jp (T.K.)
[2] School of Energy Engineering, Yulin University, Yulin 719100, China
[3] School of Electrical Energy and Power Engineering, YangZhou University, Yangzhou 225127, China; jiangwei@yzu.edu.cn
* Correspondence: hashimotos@gunma-u.ac.jp; Tel.: +81-0277-30-1741

Received: 15 September 2020; Accepted: 23 October 2020; Published: 26 October 2020

Abstract: A switching sequence model predictive direct torque control (MPDTC) of IPMSMs for EVs in switch open-circuit fault-tolerant mode is studied in this paper. Instead of selecting one space vector from the possible four space vectors, the proposed MPDTC method selects an optimized switching sequence from two well-designed switching sequences, including three space vectors, according to a new designed cost function of which the control objectives have been transferred to the *dq*-axes components of the stator flux-linkage under the maximum-torque-per-ampere control. The calculation method of the durations of the adopted space vectors in the optimized switching sequence is studied to realize the stator flux-linkage reference tracking. In addition, the capacitor voltage balance method, by injecting a dc offset to the current of fault phase, is given. Compared with the conventional MPDTC method, the complicated weighting factors designing process is avoided and the electromagnetic torque ripples can be greatly suppressed. The experimental results prove the effectiveness and advantages of the proposed scheme.

Keywords: electric vehicle; interior permanent magnet synchronous motors (IPMSMs); model predictive control; fault-tolerant

1. Introduction

The drive system of interior permanent magnet synchronous motors (IPMSMs) [1,2] based on two-level voltage source inverters (2L-VSIs) [3,4] has become one of the mainstream speed control schemes for electric vehicles (EVs) due to advantages, such as high efficiency, excellent speed regulation performance, and high power density. In order to improve the security of EVs, the functional safety of the drive system has gradually become one of the research hotspots. According to the failure mode analysis of the drive system [5], it is noted that the switch open-circuit faults of the 2L-VSI can have catastrophic consequences. In some hazardous environments, such as on highway or crowded roads, it is desirable that the 2L-VSI can continuously operate in the case of switch open-circuit failures. Thus, the fault-tolerant control of the 2L-VSI, which allows the EVs to work in the limp-home mode [6,7], is one of the key issues to ensure functional safety.

In the switch open-circuit fault-tolerant mode, the remedial methods consist of hardware and software reconfigurations. For the hardware reconfigurations, an auxiliary fourth leg is added to the 2L-VSI topology [8]. However, the cost, volume, and weight are increased, which are limited in the EV applications. Three-phase and four-switch inverters (3P4SIs) [9] can realize the switch open-circuit fault-tolerant control without increasing the cost, volume, and weight, and thus, it has outstanding advantages in the field of EVs. After an open-circuit fault is detected and located with the fault-detection strategy [10,11], the four normal switches continue to work by connecting the dc bus midpoint to the faulty phase with bidirectional thyristors.

For the software reconfigurations in the case where 3P4SIs are adopted as the fault-tolerant topology, the existing studies can be divided into three aspects according to the control strategies, i.e., flux-oriented control (FOC) with pulse-width modulation (PWM) [12–14], direct torque control (DTC) [15,16], and model predictive control (MPC) [17–22]. The above three control strategies all face the same problems, namely torque ripple suppression and capacitor voltage balance. In [12], a hybrid space vector PWM is proposed to minimize the torque ripples of the FOC by selecting optimized equivalent zero vectors. To suppress the second periodic torque ripple caused by the fluctuations of the capacitor voltages of the dc-link, a proportional integral resonant (PIR) controller is utilized for the FOC method [13]. In [14], the current reconstruction strategy using a single current sensor for 3P4SIs with FOC is studied and the errors of the sampled currents are compensated according to the current change rates under different voltage vectors. Owing to one phase winding being directly connected with the dc-link midpoint during the operation of 3P4SIs, it has been found that the predicted stator flux imbalance of DTC may be caused by unbalanced inverter voltage drop in [15], which will increase the torque ripple. A compensation scheme considering the forward voltage-drop of the switches is proposed for the DTC of 3P4SIs.

MPC strategies have the ability to deal with system constraints, multi-objective optimization, and multivariable control problems, and have been widely used in the control of power electronic converters. For the conventional MPC methods, the future values of the state variable are predicted and the space vector that minimizes the predesigned cost function is selected [17,18]. However, there are some problems to be solved for the conventional MPC methods. Firstly, the number of the space vectors has been decreased from seven to four in the switch-open fault-tolerant mode, and it is difficult to ensure the multi-objective control performance by selecting only one space vector from four space vectors, which will cause serious torque, flux, and current ripples. Secondly, the design process of the weighting factors in the cost function is complicated owing to the dimensions of the control objectives not being identical. Thirdly, the switching frequency of the conventional MPC is usually far smaller than the sampling frequency and it is not fixed, which makes the filter design complicated. An improved MPC for 3P4SIs connected to surface permanent magnet synchronous generators by increasing the adopted space vectors is studied in [19] to minimize the current reference tracking error. A 3P4SI operation of the grid-side converter of the doubly fed induction generator with the three-vector MPC strategy is studied in [20], where three space vectors are adopted to decrease the ripples of the control variables and make the switching frequency fixed. However, the methods in [19,20] are complicated to implement and the corresponding control strategy for IPMSMs has not been studied. To avoid the complicated weighting factor tuning work, a simplified model predictive flux control with capacitor voltage offset suppression for 3P4SIs is proposed in [21], and the stator flux-linkage is taken as the only control term in the cost function. An improved model predictive flux control based on the $i_d = 0$ control mode is studied in [22], where a reference stator flux vector is obtained to represent the reference flux, the reference torque, and the capacitor voltage offset. Nevertheless, the methods in [21,22] only adopt one space vector in a single control period, and the electromagnetic torque ripples reduction has not been considered. For EVs where IPMSMs are coupled to gearboxes, the electromagnetic torque ripples can excite gearbox oscillations, which may seriously reduce the driving comfort.

In this paper, a switching sequence model predictive direct torque control (MPDTC) of IPMSMs for EVs in switch open-circuit fault-tolerant mode is proposed. The stator flux-linkage reference calculation method under maximum-torque-per-ampere (MTPA) control is given. Two switching sequences including three space vectors are designed according to the features of the space vector diagram. Instead of selecting one space vector from the possible four space vectors, the proposed MPDTC method selects an optimized switching sequence from the well-designed two switching sequences according to a new designed cost function without weighting factors. Then, the durations of the adopted space vectors in the optimized switching sequence are calculated to realize the stator flux-linkage reference tracking. In addition, the capacitor voltage balance method by injecting a dc offset to the current of fault phase is studied. Compared with the conventional MPDTC method, the complicated weighting factors designing process is avoided and the electromagnetic torque ripples can be greatly suppressed. An experimental prototype is established, and the experimental results prove the effectiveness and advantages of the proposed scheme.

2. Conventional MPDTC of IPMSM for EV in Switch Open-Circuit Fault-Tolerant Mode

The speed regulation system of EVs on the basis of IPMSMs is shown in Figure 1a, where V_{dc} is the dc-link voltage; C_1 and C_2 are the upper and lower capacitors; and S_j and S_{j1} ($j = a, b, c$) are the up and low switches, which are composed of insulated gate bipolar transistors (IGBTs) and antiparallel diodes. The energy of the lithium battery pack is transmitted to the IPMSM through the 2L-VSI. To realize the fault-tolerant control of switch-open-circuit fault, three bi-directional thyristors K_a, K_b, and K_c are added between the middle point of the dc-link capacitors ('o' as defined in Figure 1a) and the output terminal of the VSI. In normal operation mode, K_a, K_b, and K_c are all in off state, and when one of the phases has an open-circuit fault, the bidirectional thyristor of the corresponding phase is closed, and the output terminal of the fault phase is connected to the middle point of the dc-link capacitors to realize the circuit reconstruction. As an example, the equivalent fault-tolerant circuit in the case where either S_a or S_{a1} is open is shown in Figure 1b, which is the so-called 3P4SI.

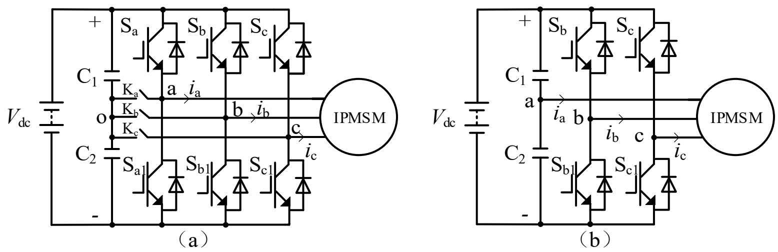

Figure 1. Speed regulation system of EVs on the basis of IPMSMs (**a**) 2L-VSI (**b**) 3P4SI.

In Figure 1b, the terminal voltage of phase a is 0 because it is directly connected to the midpoint of the dc-link capacitors, while for phases b and c, the terminal voltage is equal to the voltage of C_1 (V_{c1}) with S_j switching on, and it is equal to the negative voltage of C_2 (-V_{c2}) with S_j switching off. The switching states are defined as '1' and '0' for the former and latter cases, respectively. The combination of the switching states of phases b and c, as shown in Figure 2b, can form four space vectors in the two-phase static coordinate system (α-β), i.e., V_1–V_4. In Figure 2b, it is assumed that V_{c1} is equal to V_{c2}. Taking V_2 as an example, the corresponding switching state of phase b is 1 and the one of phase c is 0. By comparing the space vector diagrams in normal mode and in switch-open fault-tolerant mode as shown in Figure 2, the number of space vectors was decreased from 7 to 4.

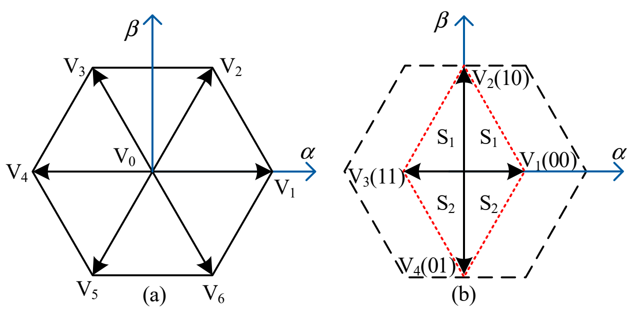

Figure 2. Space vector diagrams. (**a**) In normal mode. (**b**) In switch-open fault-tolerant mode.

The voltage and flux equations of IPMSMs are given in (1) and (2), where u_d/u_q, i_d/i_q, L_d/L_q, Ψ_d/Ψ_q, are the dq-axes voltages, currents, inductances, and stator flux-linkages, respectively, R_s is the stator resistance, ω_e is the electric angular velocity, and Ψ_f is the permanent magnet flux linkage:

$$\begin{bmatrix} u_d \\ u_q \end{bmatrix} = R_s \begin{bmatrix} i_d \\ i_q \end{bmatrix} + \begin{bmatrix} L_d & 0 \\ 0 & L_q \end{bmatrix} \frac{d}{dt} \begin{bmatrix} i_d \\ i_q \end{bmatrix} + \begin{bmatrix} -\omega_e L_q i_q \\ \omega_e L_d i_d + \omega_e \Psi_f \end{bmatrix}, \tag{1}$$

$$\begin{bmatrix} \Psi_d \\ \Psi_q \end{bmatrix} = \begin{bmatrix} L_d & 0 \\ 0 & L_q \end{bmatrix} \begin{bmatrix} i_d \\ i_q \end{bmatrix} + \begin{bmatrix} \Psi_f \\ 0 \end{bmatrix}. \tag{2}$$

The current predictive equations can be obtained by discretizing (1) and they are given in (3) and (4), where T_s is the sampling period and k is the number of T_s:

$$i_{\mathrm{d}}(k+1) = \left(1 - R\frac{T_s}{L_d}\right) i_d(k) + \omega_e T_s i_q(k) \frac{L_q}{L_d} + \frac{T_s}{L_d} u_d(k), \tag{3}$$

$$i_q(k+1) = \left(1 - R\frac{T_s}{L_q}\right) i_q(k) - \omega_e T_s i_d(k) \frac{L_q}{L_d} + \frac{T_s}{L_q} u_q(k) - \omega_e T_s \frac{\omega_f}{L_q}. \tag{4}$$

Substituting (3) and (4) into (2), the stator flux-linkage predictive equations are given in (5) and (6):

$$\Psi_d(k+1) = L_d i_d(k+1) + \Psi_f, \tag{5}$$

$$\Psi_q(k+1) = L_q i_q(k+1). \tag{6}$$

Then, the amplitude of the stator flux-linkage is calculated as follows:

$$\Psi_s(k+1) = \sqrt{\Psi_d(k+1)^2 + \Psi_q(k+1)^2}. \tag{7}$$

In addition, the electromagnetic torque can be predicted according to (8), where P_n is the pole pairs:

$$T_e(k+1) = 1.5 P_n i_q(k+1)\left[\Psi_f + \left(L_d - L_q\right) i_d(k+1)\right]. \tag{8}$$

Because the midpoint of the dc-link capacitors is connected with phase a, the difference between the voltage of C_1 and C_2 (V_{c_e}) can be calculated by (9):

$$C\frac{d(V_{c1} - V_{c2})}{dt} = C\frac{dV_{c\_e}}{dt} = i_a, \tag{9}$$

where V_{c1}, V_{c2} are the voltage of C_1 and C_2, and i_a is the current of phase 'a'. Then, the predictive equation of V_{c_e} is given in (10):

$$V_{c\_e}(k+1) = V_{c\_e}(k) + i_a \frac{T_s}{C}. \tag{10}$$

For the conventional MPDTC of IPMSMs for EVs in switch-open fault-tolerant mode, the controlled variables, including the stator flux, the electromagnetic torque, and the difference between the voltage of C_1 and C_2 for the four space vectors as shown in Figure 2b, are predicted according to (7), (8), and (10), respectively. Then, the cost function as given in (11) is calculated for each prediction, where T_e^*, Ψ_s^* are the reference of electromagnetic torque and stator flux; and λ_1, λ_2, and λ_3 are the weighting factors. At last, the space vector that minimizing the cost function is selected as the optimized solution:

$$g = \lambda_1 \left| T_e^* - T_e(k+1) \right| + \lambda_2 \left| \Psi_s^* - \Psi_s(k+1) \right| + \lambda_3 \left| V_{c\_e} \right|. \tag{11}$$

However, there are some drawbacks for the conventional MPDTC method. Firstly, the number of space vectors has been decreased from 7 to 4 in the switch-open fault-tolerant mode, and the torque and flux ripples become a serious problem owing to the number of the selectable space vectors to optimize the three objectives in (11) has been decreased by 42.85%. Secondly, the design process of λ_1, λ_2, and λ_3 is complicated owing to the dimensions of T_e, Ψ_s, and V_{c_e} not being identical. Thirdly, the switching frequency of the conventional MPDTC is usually far smaller than the sampling frequency ($1/T_s$) and it is not fixed, which makes the filter design complicated.

3. Switching Sequence MPDTC of IPMSM for EV in Switch Open-Circuit Fault-Tolerant Mode

3.1. Stator Flux-Linkage Calculation under MTPA Control

The electromagnetic torque equation is given in (12) with a simplified form, where T_{en}^*, i_{dn}, and i_{qn} can be calculated by (13). The base value of the current and electromagnetic torque is defined in (14):

$$T_{en}^* = i_{qn}(1 - i_{dn}), \tag{12}$$

$$\begin{cases} T_{en}^* = T_e^*/T_{eB} \\ i_{dn} = i_d/I_B \\ i_{qn} = i_q/I_B \end{cases}, \tag{13}$$

$$\begin{cases} I_B = \Psi_f/\left(L_q - L_d\right) \\ T_{eB} = 1.5P_n\Psi_f I_B \end{cases}. \tag{14}$$

The efficiency of the speed control system is one of the key indicators of EVs, which is of great significance to the improvement of driving mileage and energy saving. Efficiency optimization of IPMSMs is achieved through MTPA control, of which the relationship between T_{en} and i_{dn} can be obtained in (15) by making $\partial T_{en}^*/\partial i_{dn}$ equal to 0:

$$\left|T_{en}^*\right| = \sqrt{i_{dn}(i_{dn} - 1)^3}. \tag{15}$$

To realize the MTPA control, the inverse function of (15) is needed. However, it is hard to obtain the analytic formula owing to (15) is a high-order nonlinear equation. A fitting function as shown in (16) is given to calculate i_{dn} with a specific T_{en}^*. Both the MTPA and the fitting curves are plotted in Figure 3, and the two curves are nearly in coincidence, which indicates the effectiveness of the fitting function:

$$i_{dn} = \begin{cases} 0, \left|T_{en}^*\right| \le 0.02 \\ -0.7272(T_{en}^*)^2 - 0.0403T_{en}^* + 0.0013, \left|T_{en}^*\right| \le 0.24 \\ 0.0284(T_{en}^*)^2 - 0.4769T_{en}^* + 0.0694, \left|T_{en}^*\right| \le 1.3 \\ 0.039(T_{en}^*)^2 - 0.4828T_{en}^* + 0.0612, else \end{cases}, \tag{16}$$

$$i_{dn} = \begin{cases} 0, \left|T_{en}^*\right| \le 0.02 \\ -0.7272(T_{en}^*)^2 - 0.0403T_{en}^* + 0.0013, \left|T_{en}^*\right| \le 0.24 \\ 0.0284(T_{en}^*)^2 - 0.4769T_{en}^* + 0.0694, \left|T_{en}^*\right| \le 1.3 \\ 0.039(T_{en}^*)^2 - 0.4828T_{en}^* + 0.0612, else \end{cases}. \tag{17}$$

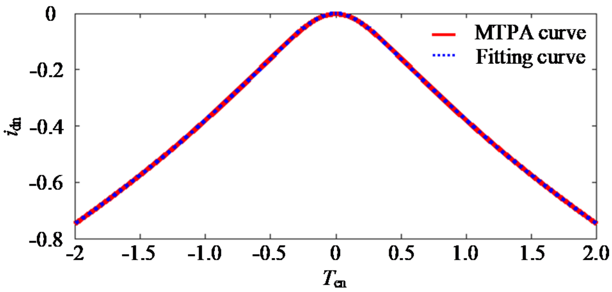

Figure 3. MTPA and the fitting curve.

After calculating i_{dn}, i_{qn} can be obtained by (17) according to (12):

$$i_{qn} = T_{en}^{*}/(1 - i_{dn}). \tag{18}$$

Furthermore, the stator flux-linkage references in the synchronous rotating coordinate axes for a specific T_e^* can be calculated by (18) and (19) to realize the MTPA control:

$$\Psi_d^* = L_d i_{dn} I_B + \Psi_f, \tag{19}$$

$$\Psi_q^* = L_q i_{qn} I_B. \tag{20}$$

That is to say, the control objectives can be transferred to Ψ_d^* and Ψ_q^* from T_e^* and Ψ_s^* under the MTPA control.

3.2. Switching Sequence Selection

In Figure 2b, the space vector diagram can be divided into 2 sectors, i.e., S_1 and S_2. Sector S_1 is above the α-axis, and it consists of V_1, V_2, and V_3. Sector S_2 is below the α-axis, and it consists of V_1, V_3, and V_4. As shown in Figure 4b,c, the positions of V_1 and V_3 are also lined in the α-axis in the case where V_{c1} is not equal to V_{c2}, and thus, the sector definition method can be applied in the three cases shown in Figure 4.

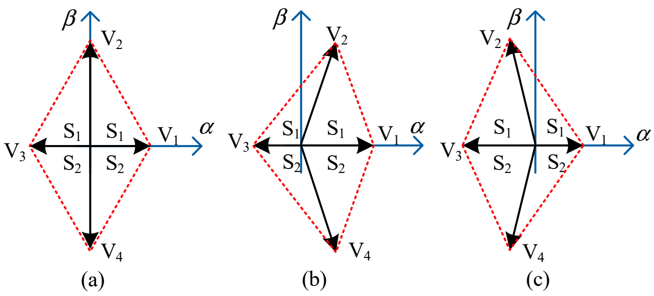

Figure 4. Space vector diagram for 3P4SI. (**a**) $V_{c1} = V_{c2}$ (**b**) $V_{c1} < V_{c2}$ (**c**) $V_{c1} > V_{c2}$.

The switching sequences in S_1 and S_2 can be designed as Figure 5 according to the nearest-three-vectors (NTVs) principle. In the sector S_1, V_1, V_2, and V_3 are selected as the NTVs, and the corresponding switching sequence is shown in Figure 5a. However, in the sector S_2, V_1, V_3, and V_4 are selected as the NTVs, and the corresponding switching sequence is shown in Figure 5b. The two cases in Figure 5a,b are defined as the switching sequence I and II, respectively.

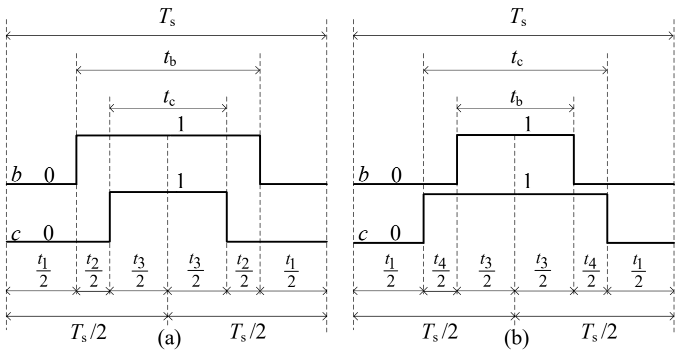

Figure 5. Switching sequence diagram (**a**) Switching sequence I (**b**) Switching sequence II.

In Figure 5, t_1–t_4 are the durations of V_1–V_4, and t_b and t_c are the durations of state '1' of phase 'b' and 'c', respectively. For the switching sequence I, t_b is bigger than t_c and the size-relation of t_b and t_c is opposite for the switching sequence II.

It can be seen from Figure 5 that both the switching sequences adopt V_1 and V_3, the difference is that the switching sequence I adopts V_2 while the switching sequence II adopts V_4. The optimized switching sequence can be selected according to (20) where a new evaluation criteria (g_1) is defined in (21). If S is I, the switching sequence I is selected; otherwise, the switching sequence II is selected:

$$S = \begin{cases} \text{I}, & g_1(V_2) < g_1(V_4) \\ \text{II}, & g_1(V_2) \geq g_1(V_4) \end{cases}, \tag{21}$$

$$g_1 = \left(\Psi_d^* - \Psi_d(k+1)\right)^2 + \left(\Psi_q^* - \Psi_q(k+1)\right)^2. \tag{22}$$

According to the part A of this section, the control objectives of tracking of T_e^* and Ψ_s^* under the MTPA control can be transferred to the tracking of Ψ_d^* and Ψ_q^*. Thus, the optimized switching sequence selecting method in (20) can ensure the optimization of the electromagnetic torque and stator flux.

3.3. Duration Calculation

After determining the switching sequence type, the durations of the adopted space vectors should be calculated to realize the tracking of Ψ_d^* and Ψ_q^*. Taking the switching sequence I as an example, Figure 6 shows one of the possible trajectories of Ψ_d and Ψ_q.

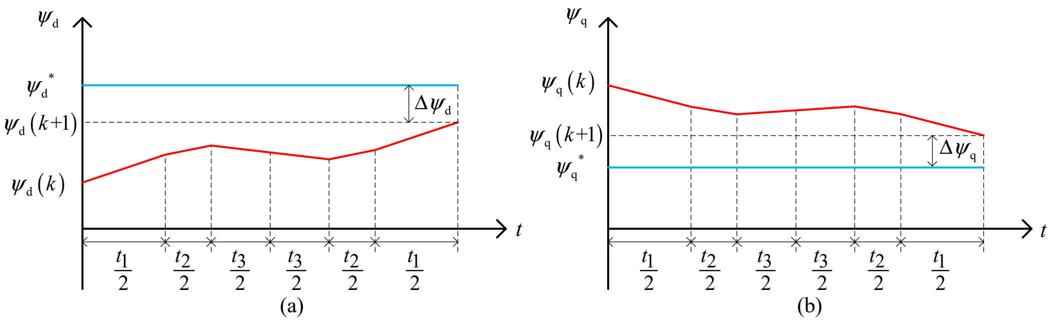

Figure 6. Trajectory of (**a**) Ψ_d and (**b**) Ψ_q with the switching sequence I.

With the switching sequence I, the difference between the reference and predicted stator flux in the synchronous rotating coordinate can be calculated by (22):

$$\begin{cases} \Delta\Psi_d = \Psi_d^* - (\Psi_d(k) + k_{1d}t_1 + k_{2d}t_2 + k_{3d}t_3) \\ \Delta\Psi_q = \Psi_q^* - \left(\Psi_q(k) + k_{1q}t_1 + k_{2q}t_2 + k_{3q}t_3\right) \end{cases}, \tag{23}$$

where k_{1d}, k_{2d}, and k_{3d} are the slopes of Ψ_d with V_1, V_2, and V_3 and k_{1q}, k_{2q}, and k_{3q} are the slopes of Ψ_q with V_1, V_2, and V_3. They can be calculated by (23) and (1):

$$\begin{cases} k_{jd} = L_d \frac{di_d}{dt}\Big|\left(u_d = V_{jd}\right) \\ k_{jq} = L_q \frac{di_q}{dt}\Big|\left(u_q = V_{jq}\right) \end{cases}, \tag{24}$$

where j = 1, 2, 3, 4 and V_{id}, V_{iq} are the d,q-axes component of space vector V_j. According to Figure 5a, (24) can be obtained:

$$\begin{cases} t_1 = T_s - t_b \\ t_2 = t_b - t_c \\ t_3 = t_c \end{cases}. \tag{25}$$

By substituting (24) in (22), (22) can be written as (25):

$$\begin{cases} \Delta\Psi_d = \Psi_d^* - (\Psi_d(k) + k_{1d}(T_s - t_b) + k_{2d}(t_b - t_c) + k_{3d}t_c) \\ \Delta\Psi_q = \Psi_q^* - \left(\Psi_q(k) + k_{1q}(T_s - t_b) + k_{2q}(t_b - t_c) + k_{3q}t_c\right) \end{cases}. \tag{26}$$

The target of the duration calculation is to determine the durations t_a and t_b in order to minimize the ripples of Ψ_d and Ψ_q under MTPA control. The optimal t_b and t_c can be obtained by minimizing the function g_2 defined in (26):

$$g_2(t_b, t_c) = (\Delta\Psi_d)^2 + \left(\Delta\Psi_q\right)^2. \tag{27}$$

Furthermore, the optimal t_b and t_c can be calculated by (27) and the results are given in (28):

$$\begin{cases} \frac{\partial g_2}{\partial t_b} = 0 \\ \frac{\partial g_2}{\partial t_c} = 0 \end{cases}, \tag{28}$$

$$\begin{cases} t_b = (m_1d_1 - b_1n_1)/(a_1d_1 - b_1c_1) \\ t_c = (a_1n_1 - c_1m_1)/(a_1d_1 - b_1c_1) \end{cases}, \tag{29}$$

where the variables in (28) satisfy (29):

$$\begin{cases} a_1 = k_{2d} - k_{1d}, \quad b_1 = k_{3d} - k_{2d} \\ c_1 = k_{2q} - k_{1q}, \quad d_1 = k_{3q} - k_{2q} \\ m_1 = \Psi_d^* - \Psi_d(k) - k_{1d}T_s \\ n_1 = \Psi_q^* - \Psi_q(k) - k_{1q}T_s \end{cases}. \tag{30}$$

For the switching sequence II, the optimal t_b and t_c can be calculated following the same principle and the results are given in (30) and (31):

$$\begin{cases} t_b = (m_2d_2 - b_2n_2)/(a_2d_2 - b_2c_2) \\ t_c = (a_2n_2 - c_2m_2)/(a_2d_2 - b_2c_2) \end{cases}, \tag{31}$$

$$\begin{cases} a_2 = k_{3d} - k_{4d}, \quad b_2 = k_{4d} - k_{1d} \\ c_2 = k_{3q} - k_{4q}, \quad b_2 = k_{4q} - k_{1q} \\ m_2 = \Psi_d^* - \Psi_d(k) - k_{1d}T_s \\ n_2 = \Psi_q^* - \Psi_q(k) - k_{1q}T_s \end{cases}. \tag{32}$$

3.4. Capacitor Voltage Balance

It can be seen from (10) that the capacitor voltage balance can be realized by injecting a dc offset to i_a. For the space vector V_1 and V_3, the output voltage of phase 'a' (V_{an}) is 2/3V_{c2} and −2/3V_{c1}, respectively. Thus, increasing the duration of V_1 (t_1) is equivalent to injecting a positive dc component into i_a, and increasing the duration of V_3 (t_3) is equivalent to injecting a negative dc component into i_a. According to Figure 5, an offset (Δt), as given in (32), can be added to t_b and t_c to adjust the durations of V_1 and V_3:

$$\begin{cases} t_b = t_b + \Delta t \\ t_c = t_c + \Delta t \end{cases}. \quad (33)$$

If Δt is positive, t_1 is decreased and t_3 is increased; it is equivalent to injecting a negative dc component into i_a and it is helpful to decrease V_{c_e}. On the contrary, it is helpful to increase V_{c_e} if Δt is negative. Accordingly, the control diagram of the capacitor voltage balance by adjusting Δt can be designed as shown in Figure 7. The dc offset of V_{c_e} is obtained by a low pass filter (LPF), and a proportional integral (PI) controller is designed to make it 0.

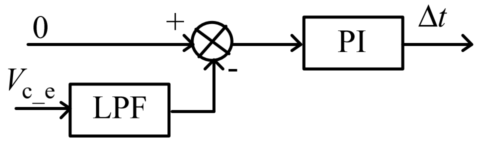

Figure 7. Diagram of capacitor voltage balancing strategy.

The whole control diagram of the switching sequence MPDTC is shown in Figure 8. With the process of stator flux calculation under MTPA control as shown in the part A, the control objectives can be transferred to Ψ_d^* and Ψ_q^* from T_e^* and Ψ_s^*, which can avoid the complicated process of adjusting λ_1, λ_2 in the conventional MPDTC. In addition, there is no need to design a cost function for the proposed capacitor voltage balance method, i.e., the design process of λ_3 in the conventional MPDTC can also be avoided. Thus, the problem of designing the weighting factors in the conventional MPDTC can be solved. Instead of selecting one space vector from V_1–V_4 as shown in Figure 4, the switching sequence with three space vectors is selected for the proposed method. The switching frequency of the proposed switching sequence MPDTC is fixed and it is equal to the sampling frequency, which is helpful to decrease the torque and flux ripples.

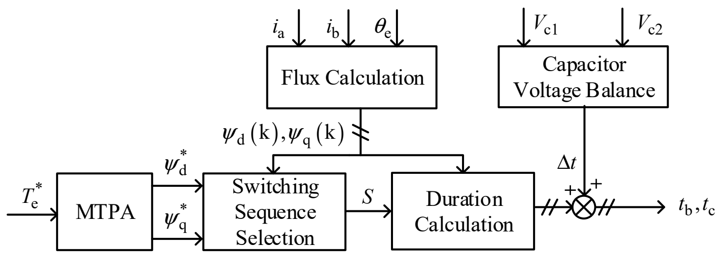

Figure 8. Control diagram of the switching sequence MPDTC.

4. Experimental Results and Discussion

4.1. Experimental Prototype

To validate the effectiveness of the proposed switching sequence MPDTC of IPMSM for EV in switch-open fault-tolerant mode, an experimental setup as shown in Figure 9 was established. A 320 V dc-link voltage is obtained by the PWM rectifier controlled by the controller 1 to simulate the lithium battery packs. IPMSM1 and IPMSM2 are coaxially connected. IPMSM1 is connected with the 3P4SI, and the proposed control strategy is implemented by the controller 3. IPMSM2 is the load motor, which is fed by the inverter 2 with controller 2. The main parameters of the 3P4SI and IPMSM1 are given in Table 1.

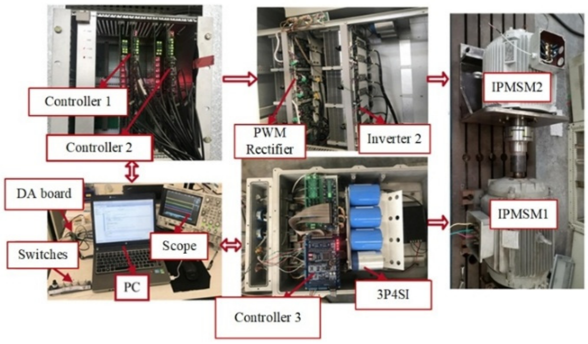

Figure 9. Experimental setup.

Table 1. Parameters of the IPMSM.

Parameter	Value
V_{dc}	320 V
C_1,C_2	4 mF
ψ_f	0.21 Wb
L_d/L_q	0.94/2.1 mH
R	0.08 Ω
Pole Pairs	4
T_s	0.0001 s
$I_{\max}$	100 A

4.2. Results and Discussion

In the experiment, the speed of IPMSM1 is controlled as 750 r/min and the load torque (T_l) is set at 50 and 100 Nm at different periods. The curves of stator flux-linkage and electromagnetic torque for the conventional method as given in [22] and the proposed MPDTC are shown in Figures 10 and 11, respectively. In the middle of Figures 10 and 11, the load torque changes from 50 to 100 Nm. It can be seen from Figure 10 that the peak-to-peak values of the stator flux-linkage ripple for the conventional MPDTC are 0.041 and 0.046 Wb with T_l set at 50 and 100 Nm, respectively. With the proposed MPDTC, the stator flux-linkage ripple has been greatly reduced. As shown in Figure 11, the peak-to-peak values of the stator flux-linkage ripple for the proposed MPDTC are 0.004 and 0.004 Wb with T_1 setting at 50 and 100 Nm, respectively. They were reduced by 90.2% and 91.3% in the two cases.

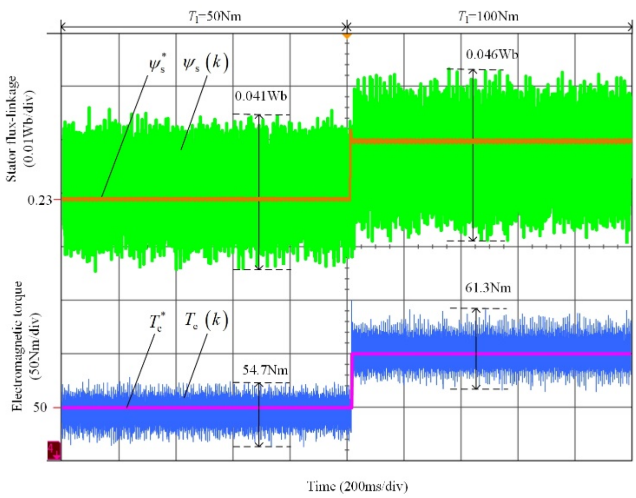

Figure 10. The curves of stator flux-linkage and electromagnetic torque for the conventional MPDTC.

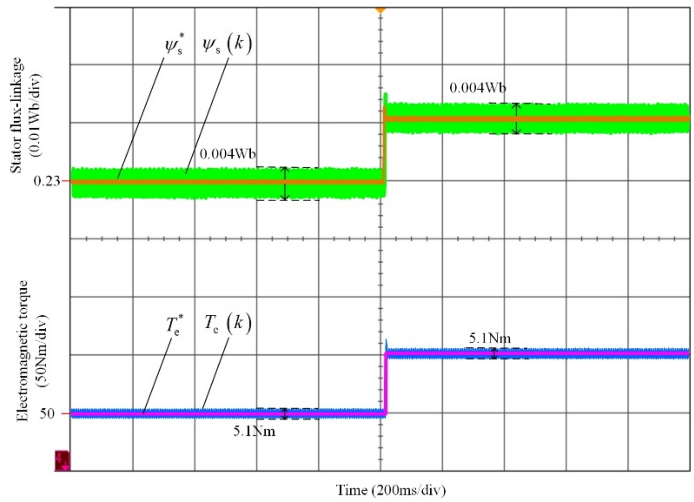

Figure 11. The curves of stator flux-linkage and electromagnetic torque for the proposed MPDTC.

In addition, the peak-to-peak values of the electromagnetic torque ripple for the conventional MPDTC, as shown in Figure 10, are 54.7 and 61.3 Nm with T_l set at 50 and 100 Nm, respectively. With the proposed MPDTC, the electromagnetic torque ripple was also greatly reduced. As shown in Figure 11, the peak-to-peak values of the electromagnetic torque ripple for the proposed MPDTC are 5.1 and 5.1 Nm with T_l set at 50 and 100 Nm, respectively. They were reduced by 90.7% and 91.7% in the two cases. In addition, both the stator flux-linkage and electromagnetic torque can be fast tracked in the load sudden change case, and thus the proposed MPDTC has an excellent dynamic performance.

The curves of the phase current with T_l set at 100 Nm for the conventional and the proposed MPDTC are shown in Figures 12 and 13, respectively. It is obvious that the current ripples were greatly reduced. The spectra of the phase current are shown in Figures 14 and 15. For the conventional MPDTC, the total harmonic distortion (THD) of the phase current is 10.35%, and it was reduced to 4.14% with the proposed MPDTC method. As shown in Figure 14, the harmonic components of the phase current concentrate on the low frequency range, mainly owing to the switching frequency of the conventional MPDTC being far smaller than the sampling frequency and it is not fixed. On the contrary, the low frequency harmonic components as shown in Figure 15 were decreased, and the harmonic order concentrate on 200, which is equal to the switching frequency of the proposed MPDTC.

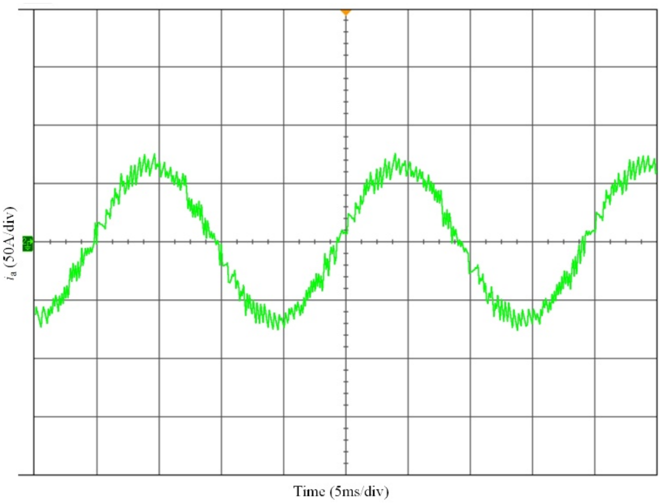

Figure 12. The curve of phase current for the conventional MPDTC.

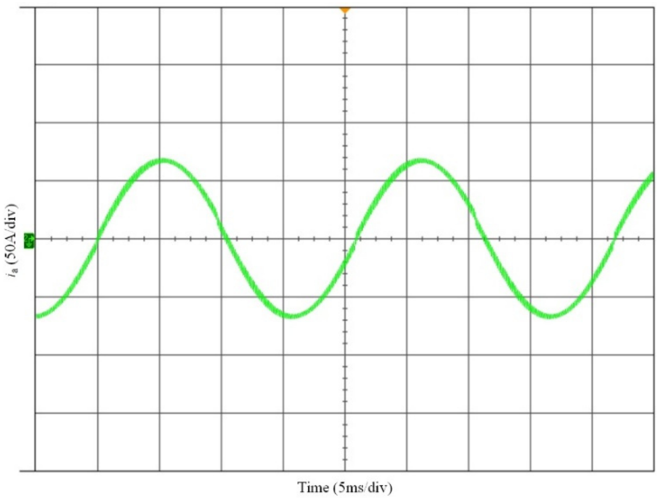

Figure 13. The curve of phase current for the proposed MPDTC.

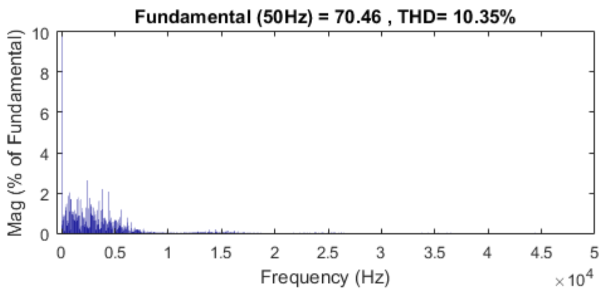

Figure 14. Spectrum of the phase current for the conventional MPDTC.

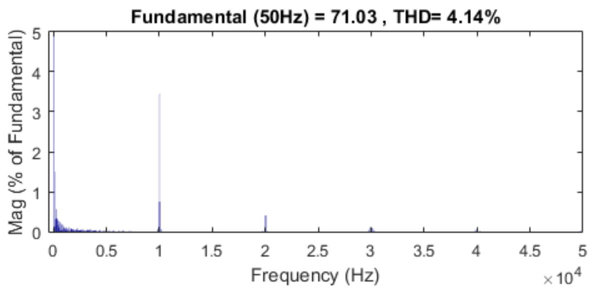

Figure 15. Spectrum of the phase current for the proposed MPDTC.

The curves of the sector and line-to-line voltage (V_{ab}, V_{ac}, V_{bc}) with T_l set at 100 Nm for the proposed MPDTC are shown in Figure 16. The line-to-line voltage curve between the two fault-free phases, i.e., V_{bc} as shown in Figure 16, is similar as the one of the 2L-VSI, while the line-to-line voltage curves between the fault-free and the fault phase were changed as V_{ac} and V_{ab} in Figure 16.

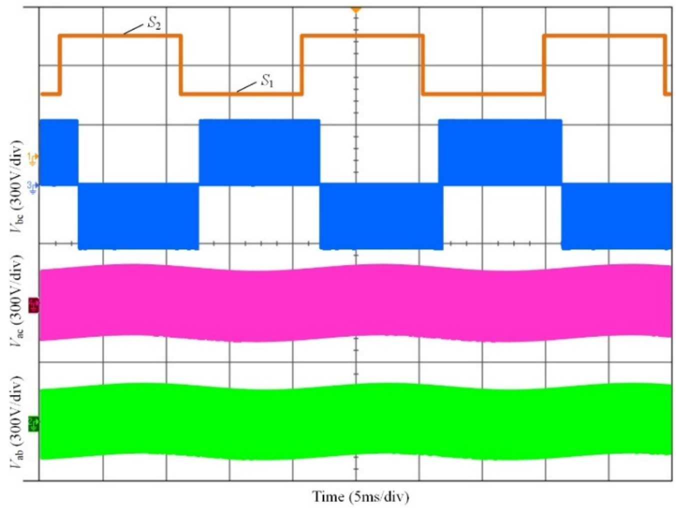

Figure 16. The curves of the sector and line-to-line voltage for the proposed MPDTC.

The curves of the capacitor voltages for the proposed MPDTC are shown in Figure 17. With the capacitor voltage balance control, both V_{c1} and V_{c2} are adjusted near 160 V.

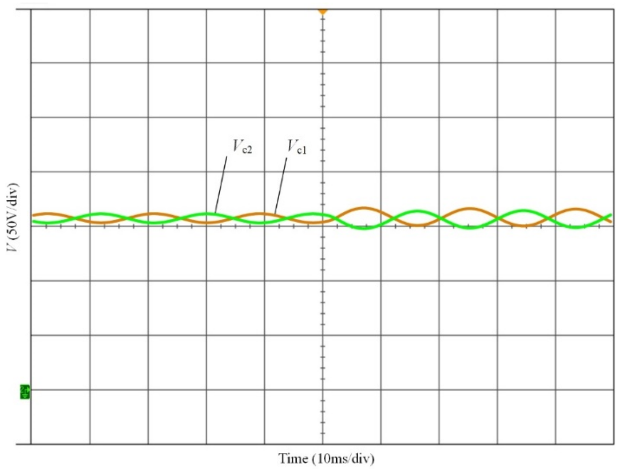

Figure 17. Curves of the capacitor voltages for the proposed MPDTC.

Accordingly, the above analysis indicates that the proposed MPDTC method is effective. Compared with the conventional method, the ripples of the stator flux-linkage, electromagnetic torque, and phase current were greatly reduced with the same sampling period.

5. Conclusions

A switching sequence MPDTC of IPMSM for EV in switch open-circuit fault-tolerant mode was studied. The control objectives were transferred to Ψ_d^* and Ψ_q^* from T_e^* and Ψ_s^* under the MTPA control. Instead of selecting one space vector from the possible four space vectors, the proposed MPDTC method selects an optimized switching sequence including three space vectors and the calculation method of the durations of the adopted space vectors is given to realize the tracking of Ψ_d^* and Ψ_q^*. The capacitor voltage balance method, by injecting a dc offset to the current of the fault phase, is also given. The experimental results indicate the effectiveness of the proposed method and the electromagnetic torque ripples were decreased by more than 90% compared with the conventional method, which is helpful to maintain the driving comfort in the open-circuit fault-tolerant mode. In the future research, the smooth transition strategy from a healthy to open-circuit fault state with a model predictive controller will be investigated.

Author Contributions: T.Y. developed the switching sequence MPDTC control algorithms and performed the experiments and analyzed the data. S.H., T.K. and W.J. guided and revised the manuscript. All authors have read and agreed to the published version of the manuscript.

Funding: This research was funded by the 2019 Special Science and Technology Research Program of the Department of Education of Shaanxi grant number [19JK1005] and Yulin College School-level Teaching Reform Research Project grant number [JG1846].

Acknowledgments: The project is partially supported by the 2019 Special Science and Technology Research Program of the Department of Education of Shaanxi Province under award 19JK1005 and is partially supported by Yulin College School-level Teaching Reform Research Project under award JG1846.

Conflicts of Interest: The authors declare no conflict of interest.

References

1. Hwang, M.-H.; Lee, H.-S.; Yang, S.-H.; Lee, G.-S.; Han, J.-H.; Kim, D.-H.; Kim, H.-W.; Cha, H.-R. Cogging Torque Reduction and Offset of Dual-Rotor Interior Permanent Magnet Motor in Electric Vehicle Traction Platforms. *Energies* **2019**, *12*, 1761. [CrossRef]
2. Chen, J.; Chen, S.; Wu, X.; Tan, G.; Hao, J. A Super-Twisting Sliding-Mode Stator Flux Observer for Sensorless Direct Torque and Flux Control of IPMSM. *Energies* **2019**, *12*, 2564. [CrossRef]
3. Wu, X.; Tan, G.; Ye, Z.; Liu, Y.; Xu, S. Optimized Common-Mode Voltage Reduction PWM for Three-Phase Voltage-Source Inverters. *IEEE Trans. Power Electron.* **2016**, *31*, 2959–2969. [CrossRef]
4. De Pinto, S.; Camocardi, P.; Chatzikomis, C.; Sorniotti, A.; Bottiglione, F.; Mantriota, G.; Perlo, P. On the Comparison of 2- and 4-Wheel-Drive Electric Vehicle Layouts with Central Motors and Single- and 2-Speed Transmission Systems. *Energies* **2020**, *13*, 3328. [CrossRef]
5. Mirafzal, B. Survey of Fault-Tolerance Techniques for Three-Phase Voltage Source Inverters. *IEEE Trans. Ind. Electron.* **2014**, *61*, 5192–5202. [CrossRef]
6. Kersten, A.; Oberdieck, K.; Bubert, A.; Neubert, M.; Grunditz, E.A.; Thiringer, T.; De Doncker, R.W. Fault Detection and Localization for Limp Home Functionality of Three-Level NPC Inverters with Connected Neutral Point for Electric Vehicles. *IEEE Trans. Transp. Electri.* **2019**, *5*, 416–432. [CrossRef]
7. Dehghanazad, E.; Gadoue, S.; Atkinson, D.J.; Slater, H.; Barrass, P.; Blaabjerg, F. Sensorless Control of IM Based on Stator-Voltage MRAS for Limp-Home EV Applications. *IEEE Trans. Power Electron.* **2018**, *33*, 1911–1921. [CrossRef]
8. Zhou, X.; Sun, J.; Li, H.; Lu, M.; Zeng, F. PMSM Open-Phase Fault-Tolerant Control Strategy Based on Four-Leg Inverter. *IEEE Trans. Power Electron.* **2020**, *35*, 2799–2808. [CrossRef]
9. Kivanc, O.; Ozturk, S. Low-Cost Position Sensorless Speed Control of PMSM Drive Using Four-Switch Inverter. *Energies* **2019**, *12*, 741. [CrossRef]
10. Li, Z.; Wheeler, P.; Watson, A.; Costabeber, A.; Wang, B.; Ren, Y.; Ma, H. A Fast Diagnosis Method for Both IGBT Faults and Current Sensor Faults in Grid-Tied Three-Phase Inverters with Two Current Sensors. *IEEE Trans. Power Electron.* **2020**, *35*, 5267–5278. [CrossRef]
11. Jlassi, I.; Cardoso, A.J.M. A Single Method for Multiple IGBT, Current, and Speed Sensor Faults Diagnosis in Regenerative PMSM Drives. *IEEE J. Emerg. Sel. Top. Power Electron.* **2020**, *8*, 2583–2599. [CrossRef]
12. Zeng, Z.; Zhu, C.; Jin, X.; Shi, W.; Zhao, R. Hybrid Space Vector Modulation Strategy for Torque Ripple Minimization in Three-Phase Four-Switch Inverter-Fed PMSM Drives. *IEEE Trans. Ind. Electron.* **2017**, *64*, 2122–2134. [CrossRef]
13. Fang, W.; Wang, Z.; Wang, D.; Li, R.; Li, M. A Strategy of Suppressing Torque Ripple in PMSM Drive System with Open-Phase Fault. In Proceedings of the 39th Chinese Control Conference, Shenyang, China, 27–29 July 2020; pp. 2573–2580.
14. Lu, J.; Hu, Y.; Liu, J. Analysis and Compensation of Sampling Errors in TPFS IPMSM Drives With Single Current Sensor. *IEEE Trans. Ind. Electron.* **2019**, *66*, 3852–3855. [CrossRef]
15. Hoang, K.D.; Zhu, Z.Q.; Foster, M.P. Influence and Compensation of Inverter Voltage Drop in Direct Torque-Controlled Four-Switch Three-Phase PM Brushless AC Drives. *IEEE Trans. Power Electron.* **2011**, *26*, 2343–2357. [CrossRef]
16. Badsi, B.E.; Bouzidi, B.; Masmoudi, A. DTC Scheme for a Four-Switch Inverter-Fed Induction Motor Emulating the Six-Switch Inverter Operation. *IEEE Trans. Power Electron.* **2013**, *28*, 3528–3538. [CrossRef]

17. Zhou, D.; Zhao, J.; Liu, Y. Predictive Torque Control Scheme for Three-Phase Four-Switch Inverter-Fed Induction Motor Drives with DC-Link Voltages Offset Suppression. *IEEE Trans. Power Electron.* **2015**, *30*, 3309–3318. [CrossRef]
18. Rivera, M.; Yaramasu, V.; Llor, A.M.; Rodriguez, J.; Wu, B.; Fadel, M. Digital Predictive Current Control of a Three-Phase Four-Leg Inverter. *IEEE Trans. Ind. Electron.* **2013**, *60*, 4903–4912. [CrossRef]
19. Zarei, M.E.; Ramirez, D.; Nicolas, C.V.; Arribas, J.R. Three-Phase Four-Switch Converter for SPMS Generators Based on Model Predictive Current Control for Wave Energy Applications. *IEEE Trans. Power Electron.* **2020**, *35*, 289–302. [CrossRef]
20. Zarei, M.E.; Nicolas, C.V.; Arribas, J.R.; Ramirez, D. Four-Switch Three-Phase Operation of Grid-Side Converter of Doubly Fed Induction Generator With Three Vectors Predictive Direct Power Control Strategy. *IEEE Trans. Ind. Electron.* **2019**, *66*, 7741–7752. [CrossRef]
21. Hua, W.; Huang, W.; Yu, F. Improved model-predictive-flux-control strategy for three-phase four-switch inverter-fed flux-reversal permanent magnet machine drives. *IET Electr. Power Appl.* **2017**, *11*, 717–728. [CrossRef]
22. Sun, D.; Su, J.; Sun, C.; Nian, H. A Simplified MPFC With Capacitor Voltage Offset Suppression for the Four-Switch Three-Phase Inverter-Fed PMSM Drive. *IEEE Trans. Ind. Electron.* **2019**, *66*, 7633–7642. [CrossRef]